



Na₂CoPO₄F as a pseudocapacitive anode for high-performance and ultrastable hybrid sodium-ion capacitors

Tyler Or^{a,1}, Karthikeyan Kaliyappan^{a,b,1}, Gaoran Li^a, Salah Abureden^a, Zhengyu Bai^b, Zhongwei Chen^{a,*}

^a Department of Chemical Engineering, University of Waterloo, 200 University Avenue West, Waterloo, Ontario, N2L 3G1, Canada

^b School of Chemistry and Chemical Engineering, Key Laboratory of Green Chemical Media and Reactions, Ministry of Education, Henan Normal University, Xinxiang, 453007, China

ARTICLE INFO

Article history:

Received 9 October 2019
Received in revised form
2 February 2020
Accepted 5 March 2020
Available online 10 March 2020

Keywords:

Na-ion capacitor
NIC
Organic electrolyte
NCPF
Activated carbon
Anode

ABSTRACT

Sodium-ion capacitors (NICs) reported in the literature demonstrate relatively poor cycle retention (<90% after 10,000 cycles) and rate performance, which is not ideal for proposed applications such as regenerative brake charging. In this work, a 3 V NIC was fabricated using Na₂CoPO₄F (NCPF) as a next-generation anode and commercial activated carbon (AC) as the cathode in an organic electrolyte. The constructed NCPF//AC NIC exhibited exceptional rate performance, retaining 78% of its energy density (corresponding to 24 Wh kg⁻¹) when the power density was ramped from 125 to 5000 W kg⁻¹. In addition, its long-term stability when cycled from 0 to 3 V is among the highest reported in the literature, retaining 93% of its energy density (24 Wh kg⁻¹) after 100,000 cycles at 1 kW kg⁻¹. Furthermore, at an elevated voltage range of 0–3.25 V, the NIC retained 80% of its energy density (26 Wh kg⁻¹) after 30,000 cycles at 375 W kg⁻¹. The performance is ascribed to the kinetic compatibility between the adsorptive cathode and pseudocapacitive anode, where pseudocapacitance is enhanced by the nanosized morphology on the surface of NCPF. The NIC system reported herein demonstrates supercapacitor-type benchmarks while also possessing a higher energy density.

© 2020 Elsevier Ltd. All rights reserved.

1. Introduction

Hybrid-ion capacitors (HICs) are designed to bridge the features of metal-ion batteries and electric double-layer capacitors (EDLCs) [1]. Typically comprised of an insertion electrode and a carbonaceous capacitive electrode in an organic (carbonate-based) electrolyte, HICs can deliver 3–4 times the energy density compared of EDLCs albeit with lower rate performance and cycle stability [1]. HICs use either lithium or sodium-based salts as charge carriers, with these devices termed lithium-ion capacitors (LICs) and sodium-ion capacitors (NICs), respectively. The operating mechanism of the device relies on the intercalation/deintercalation of Na⁺/Li⁺ with the insertion electrode while the energy storage on the capacitive electrode relies on the formation of an electric double layer through the adsorption/desorption of counter-ions (e.g., ClO₄⁻ and PF₆⁻) at the electrode-electrolyte interface [2]. The

insertion electrode contributes to the HIC energy density as it can store charge through redox pseudocapacitive (surface) and intercalation (bulk) processes, while non-Faradaic processes on the carbonaceous electrode are responsible for delivering high power density. However, the main disadvantage of this system is the mismatched kinetics between the sluggish intercalation mechanism and capacitive charge storage, resulting in poor rate performance [2]. Thus, the design, preparation, and improvement of novel insertion electrodes to match suitable capacitive electrodes is urgently required in order for HICs to be competitive in the secondary energy storage market.

A large variety of insertion electrodes for HICs have been explored and developed in the literature, such as titania-based compounds [3,4], carbonaceous electrodes [5], and transition metal oxides used as intercalation cathodes in metal-ion batteries [6–8]. Some HIC systems reported recently demonstrate an impressive energy density (upper range of 60–80 Wh kg⁻¹, normalized by active material mass), narrowing the gap in energy storage capabilities with batteries [1]. However, the vast majority of HICs still display relatively poor cycle stability and rate capability.

* Corresponding author.

E-mail address: zhwchen@uwaterloo.ca (Z. Chen).

¹ These authors contributed equally.

For instance, HICs containing titania-based insertion electrodes are desired due to their structural stability and have been optimized using nanostructuring, heteroatom doping, and carbon coating approaches in order to improve their conductivity and rate performance, but most reports demonstrate relatively poor long-term cycle stability [1]. Cycle retention loss is therefore ascribed to solid-electrolyte interphase (SEI) layer buildup and dissolution of active materials on the anode due to voltage polarization [9]. Carbonaceous insertion electrodes (e.g., hard carbon [10]) are attractive due to their ecofriendly and inexpensive composition; however, they generally showcase poor cyclability and rate performance. Cycle stability is a particularly important benchmark for HICs as their proposed applications (e.g., regenerative braking) are similar to that of supercapacitors [1]. However, while commercial supercapacitors are stable over 100,000 charge-discharge cycles, few reports in the literature on HICs demonstrate a capacity retention $\geq 90\%$ over 10,000 cycles [11–15].

While LICs have been more extensively studied, NICs are an emerging technology with its development motivated by the uneven global distribution of lithium reserves, which may cause price spikes for raw lithium materials as the demand for lithium-based batteries increases [16]. However, limited high-performance Na^+ intercalation electrodes are available due to stability issues associated with the larger ionic radius of Na^+ compared to Li^+ (0.102 nm vs 0.076 nm). Intercalation/deintercalation of Na^+ is kinetically sluggish and causes irreversible structural deformation, especially at high voltage windows. However, numerous NICs have been reported which are competitive with and even exceed the performance of most LICs in the literature [11,17,18]. This is because in addition to bulk intercalation processes, some NIC insertion electrodes possess a significant amount of pseudocapacitive charge storage contributions, which are kinetically facile and stable [19,20]. Hence, NIC technology has a promising outlook, but more work must be devoted to developing high-performance electrode materials for NICs that can deliver high energy and power density without sacrificing its cycle life.

Future energy demands require an electrode that can deliver high capacity, energy density, and high operating voltages. In this regard, sodium fluorophosphate materials ($\text{Na}_2\text{MPO}_4\text{F}$, $\text{M} = \text{Mn}, \text{Ni}, \text{Fe}$ and Co) have been proposed as potential cathode materials for NIBs [21–25]. These materials have a higher operating voltage than layered cathodes, due to the higher ionicity of the $\text{M} - \text{F}$ bond compared to $\text{M} - \text{O}$ [26]. Moreover, the highly electronegative F^- anion can charge compensate for the additional Na^+ and provide stability at high cut-off voltages [27]. They also have a high theoretical discharge capacity ($>250 \text{ mA h g}^{-1}$) assuming both Na^+ are extracted from the structure. Among the sodium fluorophosphates, $\text{Na}_2\text{CoPO}_4\text{F}$ (NCPF) has displayed a high energy density (525 Wh kg^{-1}) with a discharge plateau near 4.3 V (vs Na/Na^+) [21,22]. Few reports are available on the performance of $\text{Na}_2\text{MPO}_4\text{F}$ in half cell configuration with sodium metal anodes in organic electrolyte [21–25]. These materials showed poor cycle performance and delivered low practical capacity, demonstrating that extensive studies are required to utilize metal fluorophosphates in battery applications. However, due to the exceptionally wide operating voltage range of NCPF, we chose to assess its suitability as an insertion electrode for NICs.

In this work, we demonstrate the use of NCPF as an insertion electrode for NICs for the first time. We adopt a novel two-step synthesis technique to develop NCPF for both NIB and NIC applications. Our synthesized NCPF demonstrates promising cycle retention at the cathodic (2–5 V) and anodic (0–3 V) regions using a sodium half-cell configuration, although the initial discharge capacities were only partially reversible. The charge storage mechanism at the anodic region was primarily pseudocapacitive. Hence,

an NCPF//AC NIC was assembled for the first time using NCPF as the anode and AC as the cathode. The resulting performance was remarkable in terms of cyclic life (over 100,000 cycles) and power output, which outperforms most LICs and NICs reported in the literature.

2. Experimental

2.1. Synthesis of NCPF

Nano-sized NCPF powders were prepared by a two-step method. Initially, NaCoPO_4 (NCP) nanoparticles were synthesized using a citric acid assisted sol-gel method. Stoichiometric amounts of sodium acetate trihydrate (Sigma-Aldrich, Mississauga, Canada), cobalt(II) acetate tetrahydrate (Sigma-Aldrich), and ammonium phosphate dibasic (Sigma-Aldrich) were dissolved in deionized water with citric acid (Sigma-Aldrich) and stirred at 110°C . The molar ratio of metal ions to citric acid was fixed at 1:3. After evaporating excess water, the obtained gel precursor was decomposed at 400°C for 4 h to remove organic and ammonium moieties. The final calcination was performed at 800°C for 10 h in air to form NCP. To obtain NCPF, the NCP powder was ground with sodium fluoride (Sigma-Aldrich) using a mortar and pestle, then calcined at 750°C for 1.5 h under Ar flow, and immediately quenched to room temperature in air. The resultant NCPF was ground to a fine powder and stored in a vacuum oven. AC with a surface area of $1700 \text{ m}^2 \text{ g}^{-1}$ was purchased from Wako Chemicals (Japan) and used as received.

2.2. Physical and chemical characterization of NCPF

The phase purity of the pristine NCPF active material was assessed using powder X-ray diffraction (XRD, XRDMIniflex 600, Rigaku, Japan) with $\text{Cu K}\alpha$ radiation ($\lambda = 1.5406 \text{ nm}$) at a scan rate of $0.1^\circ/\text{min}$. Rietveld refinement was conducted on MAUD software [28] while the crystal lattice structure was generated using VESTA [29]. The morphology of the particles was observed with scanning electron microscopy (SEM, LEO Zeiss 1550, Switzerland) using a 20 kV acceleration voltage and a working distance between 8 and 9 mm coupled with energy-dispersive X-ray spectroscopy (EDX). Prior to imaging, the particles were sputtered with $\sim 5 \text{ nm}$ of gold. The valence state of the metal ions in NCPF were determined by X-ray photoelectron spectroscopy (XPS, Thermo Scientific Theta Probe, Waltham, MA, USA) using $\text{Al K}\alpha$ radiation. The binding energies reported are referenced to graphitic carbon at 284.8 eV. Thermogravimetric analysis (TGA, TA Instruments Q500, Grimsby, Canada) was conducted from 0 to 800°C at a ramp rate of $5^\circ\text{C}/\text{min}$ to detect the presence of a carbon coating. Surface area measurements were conducted by Brunauer-Emmett-Teller (BET) analysis using N_2 adsorption (Gemini VII, Micromeritics, Norcross, GA, USA).

2.3. Preparation of NCPF and AC electrodes

The electrode was prepared by grinding a slurry of 70 wt% active material (NCPF or AC), 20 wt% conductive carbon black (Ketjen-black, Lion Specialty Chemical Co., Japan), and 10 wt% Teflonized acetylene black binder in ethanol using a mortar and pestle. The electrode film was pressed ($\sim 8000 \text{ kPa}$) onto a 15 mm diameter stainless steel mesh and dried overnight at 80°C in a vacuum oven. The mass loading for the active material was 6 mg cm^{-2} . In order to assemble the NIC, a 1:1 wt ratio of NCPF:AC active material was used.

2.4. Electrochemical characterization of NIC and electrode half cells

The electrochemical performance of the NCPF electrode was

assessed by assembling CR2032 coin cells in an Ar-filled glove box (O_2 and $H_2O < 0.5$ ppm, MBRAUN, Stratham, NH, USA) using a pure sodium foil as the counter electrode, a polypropylene separator (Celgard 2400, Charlotte, NC, USA), and an electrolyte comprised of 1 M $NaClO_4$ dissolved in 1:1 ethylene carbonate:diethyl carbonate (Sigma-Aldrich, 1:1 v/v). NIC cells were constructed as described above using NCPF as the anode and commercial AC (Sigma-Aldrich) as the cathode. Cyclic voltammetry (CV) and electrochemical impedance spectroscopy (EIS) curves were acquired using a Gamry Instruments potentiostat (Warminster, PA, USA). EIS measurements were conducted from 1 MHz to 100 mHz at discharged state. Long-term galvanostatic charge-discharge studies and rate performance tests were carried out at ambient temperature using a CT2001A LAND battery testing system (Wuhan, China). After long-term cycling, the coin cell was disassembled in a glove box, and the NCPF electrode was washed in ethylene carbonate, dried in a vacuum oven, and subsequently characterized via XRD, XPS, and EDX.

The cell capacitance (C_{cell}) of the NIC was calculated from the charge-discharge curves using Eq. (1):

$$C_{cell} = \frac{it}{\Delta V} \quad (1)$$

where i is the current (A), t is the discharge time (s), and ΔV is the voltage range (V). The specific discharge capacitance (C_{dc}) was then obtained using Eq. (2):

$$C_{dc} = \frac{4C_{cell}}{m} \quad (2)$$

where m is the total mass of the anode and cathode active materials. The energy (E_D , Wh kg^{-1}) and power density (P_D , W kg^{-1}) were then obtained from C_{cell} using Eqs. (3) and (4) respectively:

$$E_D = \frac{1}{2} \frac{C_{cell} \Delta V^2}{3.6} \quad (3)$$

$$P_D = \frac{E_D \times 3600}{t} \quad (4)$$

3. Results and discussion

NCPF was synthesized by a two-step process for the first time, where $NaCoPO_4$ (NCP) was first formed through a citric-acid assisted sol-gel method. The XRD pattern of NCP indicates that the structure matches the α -polymorph indexed to the $Pnma$ space group with lattice parameters $a = 8.880$, $b = 6.799$, $c = 5.035$ (Fig. S1A), which comprises octahedrally coordinated Na and Co atoms, and P tetrahedra (Fig. S1B) [30]. NCP was then reacted with NaF through a conventional solid-state method to generate NCPF.

SEM images of the synthesized NCPF powder show large primary particles with an average size of $10 \mu m$ (Fig. 1A) and at higher magnifications (Fig. 1B), nanometer-scale secondary particles are evident. This morphology is expected to increase the surface area of contact with the electrolyte, thus reducing the diffusion path of Na^+ and enhancing electrochemical performance [31]. Indeed, the BET surface area was measured as $6.3 m^2 g^{-1}$, which is higher than typical transition metal oxide electrode powders [32]. The high surface area can also be explained by the decomposition of citric acid among the NCP particles during calcination, which evolves CO and CO_2 gases and thus forms void spaces within the particles [33]. Although citric acid and acetate precursor was used, no carbon coating was present on the final NCPF particles following calcination, according to TGA measurements (Fig. S2A). The powder XRD pattern (Fig. 1C) indicates that the NCPF has an orthorhombic structure indexed to the $Pbcn$ space group with the lattice parameters $a = 5.2415 \text{ \AA}$, $b = 13.7823 \text{ \AA}$, and $c = 11.6814 \text{ \AA}$ calculated from a Rietveld refinement, corresponding with previous reports [21–23]. As seen in Fig. 1D, the structure is comprised of layers built from PO_4 tetrahedral and $Co_2O_7F_2$ bi-octahedral units, and Na^+ located in the interlayer space [23].

The high-resolution XPS spectra of the Na 1s, Co 2p, P 2p, O 1s,

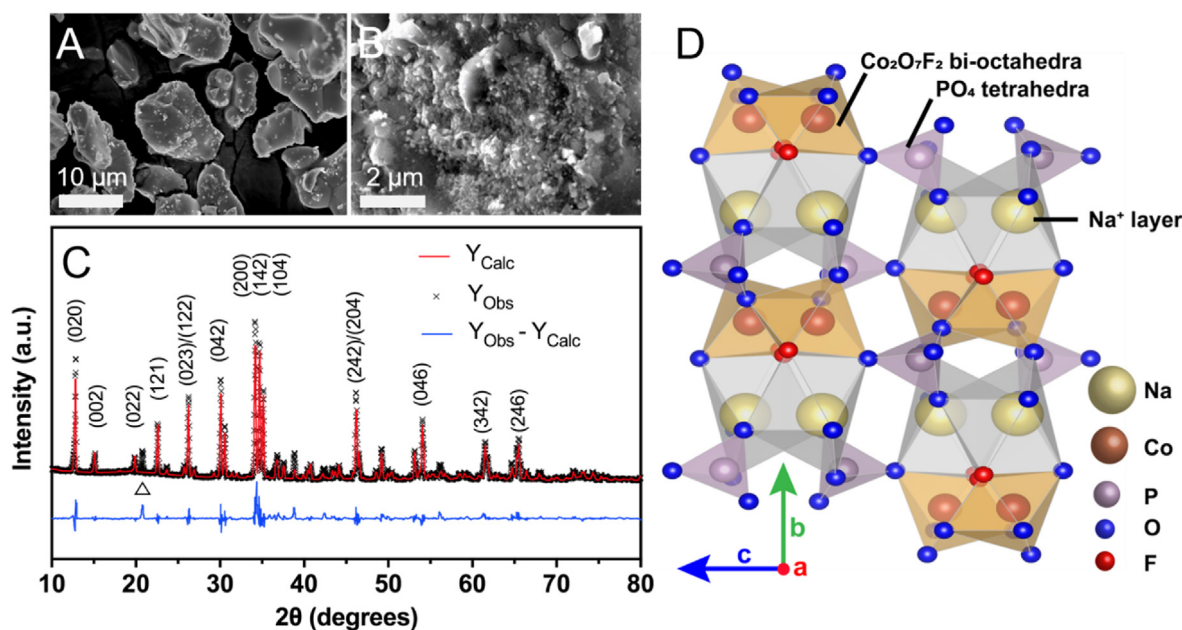


Fig. 1. Powder NCPF Characterization. A and B) SEM images of particles. C) XRD pattern with Rietveld Refinement ($R_{wp} = 13.2\%$). Δ marks location of impurity peak likely from excess sodium phosphate [40]. D) Unit cell of NCPF lattice.

and F 1s subshells of pristine NCPF is shown in Fig. S2. The Na 1s photoemission spectra (Fig. S2B) shows a peak centered at 1070.81 eV, which is in good agreement with tabulated values for Na-phosphate compounds (e.g., $\text{Na}_4\text{P}_2\text{O}_7$ at 1070.8 eV [34]). The broad and slightly asymmetric appearance of the spectra is likely due to the fact that NCPF contains two energetically inequivalent Na sites (denoted Na1 and Na2) that are difficult to distinguish as the binding energy difference is small [35]. This was similarly observed in $\text{Na}_2\text{FePO}_4\text{F}$ [36] and $\text{Li}_2\text{CoPO}_4\text{F}$ [37]. The Co 2p region (Fig. S2C) shows binding energies of 780.76 and 796.92 eV for the $2p_{3/2}$ and $2p_{1/2}$ multiplets respectively (orbital splitting of 16.2 eV) that each possess satellite peaks at 785.83 and 803.07 eV, which is characteristic of a +2 valence state [38]. It is worth mentioning that the NCPF Co $2p_{3/2}$ binding energy is upshifted compared to our synthesized NaCoPO_4 (780.32 eV). This is likely due to the presence of Co–F bonds, which possess a higher bond ionicity compared to Co–O [39]. The P 2p binding energy at 132.97 eV (Fig. S2D) corresponds to a +5 valence state, while O 1s at 530.57 eV (Fig. S2E) is similar to the values of Na_3PO_4 (530.4 eV) and CoO (530.1 eV). Like Na, F is located in two energetically inequivalent sites. The F 1s spectra (Fig. S2F) displays a broad and asymmetric appearance that is deconvoluted to reveal two peaks at 684.30 and 686.36 eV, which can be indexed to Na–F and Co–F bonds respectively [34]. The elemental composition of the synthesized NCPF was confirmed using EDX, revealing a Na:Co:P:O:F atomic ratio of 1.92:0.98:1.02:4.24:1 (Fig. S3). These characterizations confirm the successful synthesis of carbon-free NCPF.

3.1. Electrochemical characterization of NCPF

The electrochemical performance of NCPF was first assessed by assembling half cells using sodium foil as the counter electrode (Fig. 2). Due to the lack of published reports on NCPF, our half-cell performance at the anodic (0–3 V vs Na/Na^+) and cathodic (2–5 V vs Na/Na^+) region is shown in detail in Fig. 2 and Fig. S4, respectively. At the anodic region (0–3 V vs Na/Na^+), galvanostatic charge-discharge data show that the Na^+/NCPF cell has an initial discharge capacity of 130 mA h g^{-1} at 17 mA g^{-1} (0.13 C), with significant irreversible capacity loss in subsequent cycles, likely due to lattice structural changes and formation of a passivating SEI layer. Fig. S5 displays the *ex-situ* XRD pattern, which reveals significant peak broadening associated with structural defects over the first 20 cycles. The initial discharge curves (Fig. 2A) show a plateau at $\sim 1.1 \text{ V}$, likely associated with Na^+ insertion, which resulted in capacity decay and structural evolution that was observed over the preliminary cycles. However, reasonable capacity retention was maintained after 40 cycles, stabilizing at $\sim 50 \text{ mA h g}^{-1}$ (Fig. 2B). Following the irreversible capacity loss, CV curves

(Fig. 2C) show no defined peaks in the 0–3 V region. The featureless appearance of the CV curves resembles reports on amorphous pseudocapacitive materials such as MoO_3 [40] and Nb_2O_5 [19]. As the electric double-layer charge storage contribution from NCPF is considered to be negligible due to its low specific surface area, this suggests that the charge-storage mechanism is primarily based on redox pseudocapacitance on the surface of the active material. To examine this further, CV was conducted at various potential sweep rates (ν) and the current response (i) was analyzed. At the anodic peak potential ($\sim 0.75 \text{ V}$), the b -parameter (based on the relationship $i = a\nu^b$) was calculated as 1 (Fig. 2C inset), which is characteristic of a capacitive behaviour. Taken together, this suggests that the charge storage occurs within a single phase material and is not primarily based on diffusion-limited intercalation [40,41].

At the cathodic region (2–5 V vs Na/Na^+), an initial discharge capacity of 120 mA h g^{-1} at 22 mA g^{-1} (0.18 C) was obtained with subsequent irreversible capacity loss until it stabilized at $\sim 50 \text{ mA h g}^{-1}$ after 50 cycles (Fig. S4A). A discharge capacity of 42 mA h g^{-1} was retained after 200 cycles. It should be noted this cycle stability is remarkable for such a high voltage cut-off compared to other NCPF reports [21,22]. For instance, NCPF synthesized by Zou et al. displayed an initial discharge capacity of 107 mA h g^{-1} at 61 mA g^{-1} and decayed rapidly to 40 mA h g^{-1} after 20 cycles [22]. CV curves (Fig. S4C) show a small anodic peak at $\sim 3.9 \text{ V}$ and a broad cathodic peak at $\sim 3.6 \text{ V}$ during the first cycle associated with the $\text{Co}^{2+}/\text{Co}^{3+}$ redox. Subsequent cycles display a broad anodic peak at $\sim 3.4 \text{ V}$ and two cathodic peaks at $\sim 2.8 \text{ V}$ and $\sim 3.8 \text{ V}$. This implies significant structural changes during the initial cycling, where the two cathodic peaks represent Na^+ insertion sites of different local environments [42]. It should be noted that the discharge curves appear different compared to previous reports on NCPF due to the lack of a distinct discharge plateau at $\sim 4.3 \text{ V}$ for the $\text{Co}^{2+}/\text{Co}^{3+}$ redox reaction [21,22]. This difference can be ascribed to the unique synthesis approach in this work. As mentioned, we used a two-step method where NaCoPO_4 was first synthesized by a conventional sol-gel method, followed by a solid-state reaction with NaF. The sloping appearance of the discharge curve resembles that of NaCoPO_4 , suggesting that the difference is associated with the distribution of F atoms in the structure [42]. This helps explain the lower onset potential of the $\text{Co}^{2+}/\text{Co}^{3+}$ redox reaction. However, this was not distinguished in the powder characterization so the exact mechanisms are a subject for future exploration. The coulombic efficiency was low ($\leq 80\%$) throughout cycling, which is commonly observed due to accelerated decomposition of the carbonate-based electrolyte at high cut-off potentials [32]. Based on the half-cell electrochemical data, NCPF was chosen as an insertion anode to construct the NIC system along with an AC cathode.

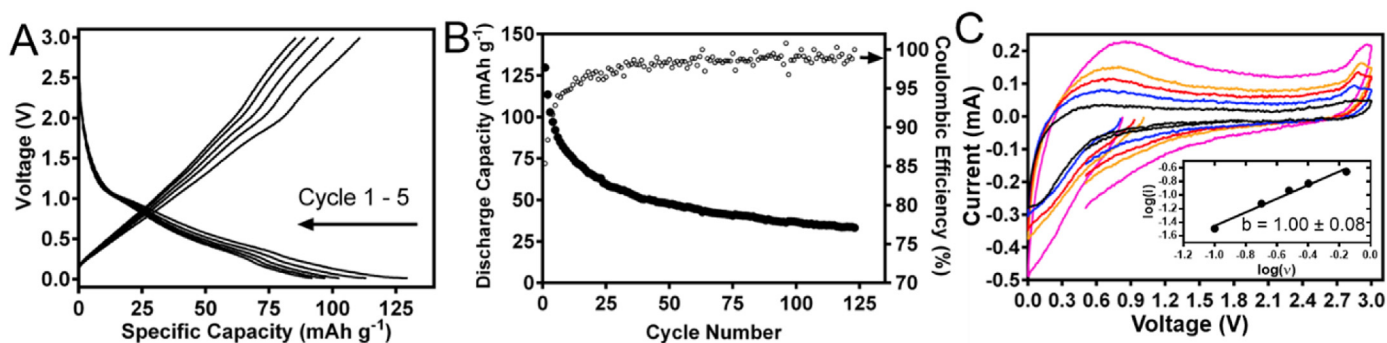


Fig. 2. Half-cell characterization of NCPF anode cycled from 0 to 3 V vs Na/Na^+ at 22 mA g^{-1} current. A) First five charge-discharge curves. B) Discharge capacity retention through 120 cycles. C) CV curves measured with various sweep rates (ν) from 0.1 to 0.7 mV s^{-1} .

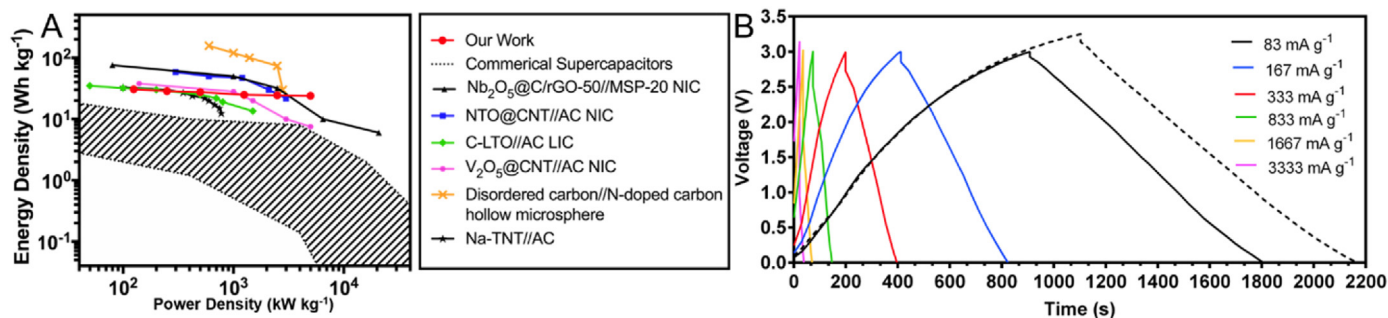
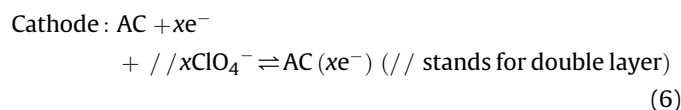
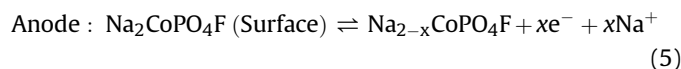


Fig. 3. Rate performance of NCPF//AC NIC cycled from 0 to 3 V. A) Ragone plot comparison of our NCPF//AC system with notable HICs in the literature[20,44–48] and commercial supercapacitors.[49] Energy and power density are normalized by the total mass of the active materials. Data for commercial supercapacitors was converted from device to active material normalized energy density by multiplying the values by four.[50] B) Initial charge-discharge curves at various currents. The dashed curve was measured from 0 to 3.25 V at 83 mA g⁻¹.

The assembled NCPF//AC NIC was tested at two potential ranges (0–3 V and 0–3.25 V) at various current densities using 1 M NaClO₄ electrolyte. Although a 3 V window is a typical benchmark for HICs, 3.25 V was also explored to expand the energy density of the device. CV curves of the NIC at different scan rates (Fig. S6) show characteristic rectangular-like plots that retain their shape from 3 to 50 mV s⁻¹, indicating good charge propagation within the electrodes and no noticeable polarization. As seen in Fig. 3B, the charge-discharge profiles at various currents deviate slightly from triangular curves observed in ideal supercapacitors, due to the combination of Faradaic and non-Faradaic charge-storage processes.

The expected reaction mechanism in the cell is shown in Eqs. (5) and (6) below:



During charging, Na-ions adsorb on the surface of NCPF where they are reduced. To relieve the charge imbalance, ClO₄⁻ ions simultaneously adsorb onto the surface of AC to form an electric double-layer. During discharge, the reverse occurs where Na⁺ is released into the electrolyte and ClO₄⁻ quickly desorbs from AC.

The assembled NICs were initially cycled at 83 mA g⁻¹ (pre-cycling) until the cell capacitance stabilized after ~200 cycles with a ~60% loss of the initial capacitance. Following pre-cycling, the rate performance was assessed from 0 to 3 V at current densities of 83, 167, 333, 833, 1667, and 3333 mA g⁻¹. A Ragone plot (Fig. 3A) was generated by averaging the energy density calculated at each current over 125 cycles. The NCPF//AC system retained 78% of its energy density from 125 to 5000 W kg⁻¹. At low currents, the energy density of the NCPF//AC device is higher than commercial supercapacitors but lower than HICs recently reported in the literature. However, the energy density surpasses most HICs at high currents (24 Wh kg⁻¹ at 5 kW kg⁻¹). Fig. 3B displays the initial charge-discharge curves at these currents, where it is clear that the voltage (IR) drop at the charge-discharge transition is unpronounced even at high currents, indicating a low device internal resistance. As long-term cycle retention is critical for the commercial development of HICs, this was then assessed from 0 to 3 V at 250 mA g⁻¹, displaying an initial specific capacitance of 90 F g⁻¹ (28 Wh kg⁻¹) with a retention of 94% over 10,000 cycles.

The cycle performance was extended at higher current with little compromise in energy density due to the excellent rate performance. At 667 mA g⁻¹, the NCPF//AC NIC retained ~93% of its initial capacitance (corresponding to 24 Wh kg⁻¹) after 100,000 cycles (Fig. 4A). This stability is among the highest ever reported for HICs (i.e., both LICs and NICs) as compared in Table 1. Fig. 4B displays the charge-discharge curves during the initial (following pre-cycling) and final cycles of this sample. The shapes of the curves appear well retained, and the voltage drop at the charge-discharge transition appeared consistent, suggesting minimal changes in internal resistance of the device throughout cycling. In the interest of expanding the energy density, the cyclability from 0 to 3.25 V was assessed. The cell displayed an initial capacitance of 96 F g⁻¹ (35 Wh kg⁻¹) and remarkably, 88% of the capacitance was retained after 10,000 cycles at 250 mA g⁻¹, eventually decaying to 80% after 30,000 cycles (Fig. 4D). This is among the highest stability ever reported for a voltage window >3 V (Table 1). It should be noted that despite the poorer stability at a 3.25 V window, the energy density after 10,000 cycles (29 Wh kg⁻¹) still exceeded that of the 3 V window sample (26 Wh kg⁻¹) at 250 mA g⁻¹.

It is typically observed in HICs that at higher charge-discharge rates, ion diffusion into the pores of active materials is reduced, and thus the charge storage mechanism is primarily dictated by surface phenomena as opposed to bulk processes [12]. Thus, cyclability is improved at higher current, as bulk processes can cause lattice strain in the insertion anode, resulting in irreversible capacity loss. This was clearly observed in our long-term cycling results when comparing the samples cycled from 0 to 3 V at 250 mA g⁻¹ vs 667 mA g⁻¹. However, due to the loss of bulk charge-storage contributions, the energy density should decrease at high rates. The fact that our NIC system displays an excellent rate performance supports our earlier observations that the charge storage mechanism in NCPF when functioning as an anode is mostly pseudocapacitive, and thus its kinetics can match the high-rate adsorption cathode. However, it should be noted that the energy density retention and cyclability at high current was poor when tested from 0 to 3.25 V (data not shown). A similar trend was observed in other reports when the voltage window was expanded [4,43]. This is likely caused by voltage polarization effects that become more prevalent at high currents, resulting in accelerated SEI layer formation at the anode and capacity throttling at the cathode [9]. As discussed, the excellent long-term cyclability and rate performance of the NIC device (Table 1) is ascribed to the pseudocapacitive charge-storage mechanism of the NCPF anode. Charge storage is aided by the nanometer-scale features of the particles that increase the active surface area for redox reactions. Due to the structural evolution and peak broadening of the NCPF

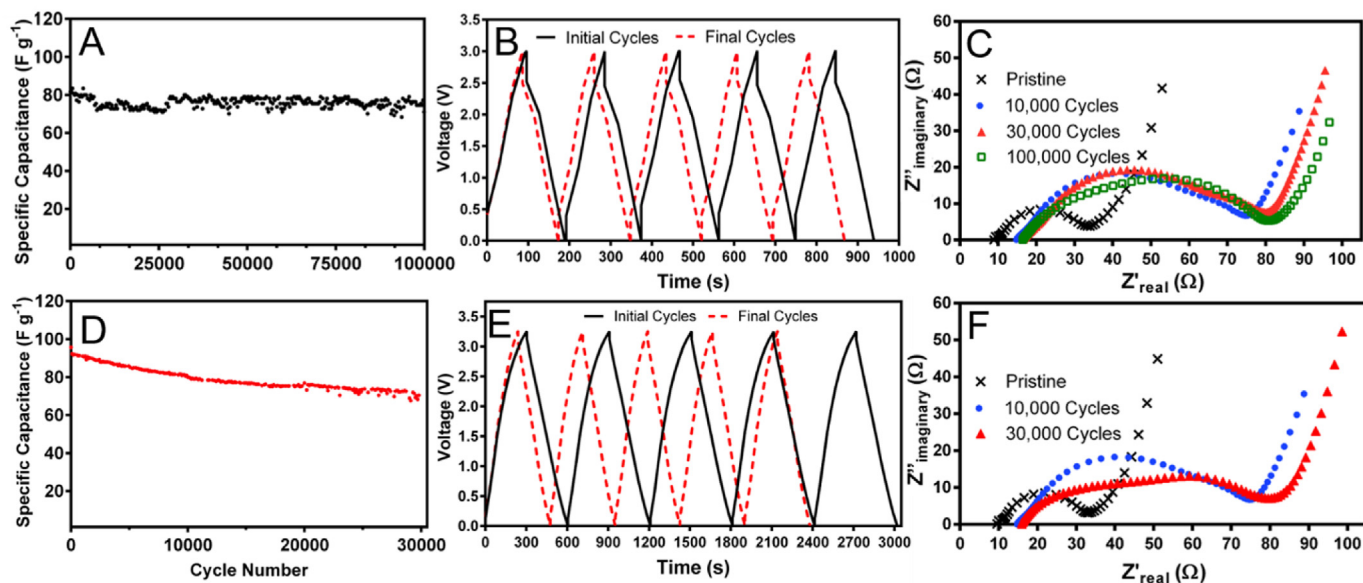


Fig. 4. Electrochemical performance of NCPF//AC NIC. Long-term cycle stability (A and D), initial (black solid) and final (red dotted) charge-discharge curves (B and E), and EIS spectra (C and F) of samples cycled from: A–C) 0–3 V at 667 mA g^{-1} and D–F) 0–3.25 V at 250 mA g^{-1} . (For interpretation of the references to colour in this figure legend, the reader is referred to the Web version of this article.)

Table 1
Comparison of cycle stability of NCPF//AC with notable NICs and LICs in the literature.

HIC System (Anode//Cathode)	Voltage Range Tested	Cycle Stability
Our work – NCPF//AC NIC	0–3 V	93% after 100,000 cycles at 0.67 A g^{-1}
Our work – NCPF//AC NIC	0–3.25 V	80% after 30,000 cycles at 0.25 A g^{-1}
$\text{Nb}_2\text{O}_5/\text{C}/\text{rGO}-50//\text{MSP}-20$ NIC [46]	1–4.3 V	66% after 3000 cycles at 1 A g^{-1}
Nb_2O_5 nanosheets//Peanut shell AC NIC[56]	1–3 V	80% after 3000 cycles at 1.28 A g^{-1}
PSNC3-800//PSOC-A NIC [10] (carbonaceous electrodes derived from peanut shells)	1.5–4.2 V	72% after 10,000 cycles at 6.4 A g^{-1}
$\text{LiNi}_{0.5}\text{Mn}_{1.5}\text{O}_4//\text{AC}$ LIC [6]	1.5–3.25 V	81% after 3000 cycles at 1 A g^{-1}
$\text{NaTi}_2(\text{PO}_4)_3//\text{AC}$ NIC [17]	0.01–2.5 V	~100% after 20,000 cycles at 5 A g^{-1}
$\text{Mo}_{0.1}\text{Ti}_{0.9}\text{O}_2//\text{AC}$ LIC [4]	1–3 V	75% after 5250 cycles at 5 mA cm^{-2} or 3.7 mA g^{-1}
$\text{Na}_3\text{V}_2(\text{PO}_4)_3//\text{AC}$ NIC [12]	0–3 V	95% after 10,000 cycles at 1.1 mA cm^{-2}
$\text{NaTi}_2(\text{PO}_4)_3/\text{GNs}/\text{GNs}$ NIC [11]	0–3 V	90% after 75,000 cycles at 4 A g^{-1}
$\text{V}_2\text{O}_5/\text{CNT}/\text{AC}$ LIC[57]	0–2.7 V	78% after 10,000 cycles at 30 C or 820 W kg^{-1}
TiC//N-doped carbon LIC[58]	0–4.5 V	82% after 5000 cycles at 2 A g^{-1}
$\text{TiO}_2/\text{Carbon}/\text{Nanoporous carbon}$ NIC [15]	1–4 V	90% after 10,000 cycles at 1 A g^{-1}
$\text{Zn}_{0.25}\text{V}_2\text{O}_5/\text{rGO}/\text{Mesoporous carbon}$ NIC[59]	1–3.8 V	87% after 2000 cycles at 1 A g^{-1}
$\text{MoSe}_2/\text{Graphene}/\text{AC}$ NIC[60]	0.5–3 V	81% after 5000 cycles at 5 A g^{-1}
Disodium rhodizonate//Cardamom shell-derived porous carbon NIC[61]	0–3 V	85% after 10,000 cycles at 4 A g^{-1}
$\text{Na}_{0.66}\text{Mn}_{0.54}\text{Ni}_{0.13}\text{Co}_{0.13}\text{O}_2-\text{Al}_2\text{O}_3//\text{AC}$ NIC [13]	0–3 V	98% after 10,000 cycles at 0.35 A g^{-1}
PPy// $\text{V}_2\text{O}_5//\text{AC}$ aqueous hybrid capacitor [14]	0–1.8 V	95% after 10,000 cycles at 10 C
$\text{Co}_x\text{Ni}_{1-x}(\text{OH})_2/\text{rGO}/\text{PPD}-\text{rGO}$ aqueous hybrid capacitor[62]	0–1.6 V	~100% after 20,000 cycles at 20 A g^{-1}

lattice structure displayed in the half-cell *ex-situ* XRD pattern in Fig. S5, it is inferred that pseudocapacitance accounts for most of the charge-storage mechanism of NCPF in the NIC device after the irreversible capacity losses that occur during the pre-cycling stage. As pseudocapacitance is mostly a surface-controlled reaction, the reversible energy density (at low current) of our NCPF//AC system is relatively low compared to other HICs in the literature [1]. Thus, our future work aims to expand the capacitive contribution of NCPF by generating carbon-composite structures possessing unique hierarchical architectures [44].

Fig. 4C and F shows the EIS spectra of the NIC throughout long-term cycling. The spectra possess a semicircle at the high-medium frequency region followed by a straight incline at low frequency, which correspond to the electrode/electrolyte charge-transfer impedance (R_{ct}) and Warburg impedance (W) respectively [45]. The high-frequency intercept at Z'_{real} is denoted the bulk impedance (R_e) and is a sum of contributions related to the conductivity

throughout the electrolyte, electrode, and current collector. When cycling at 3 and 3.25 V windows, both samples show an increase in R_{ct} and R_e after 10,000 cycles, likely due to irreversible phase changes that impede charge transfer kinetics and the initial formation of an electrically insulating SEI layer. Cycling at a 3 V window, the R_e and R_{ct} impedances show minor increases after 30–100,000 cycles, suggesting good stability of the SEI layer and NCPF structure. However, after 30,000 cycles at 3.25 V, a second overlapped semicircle is clearly observed at the high-frequency region (Fig. 4F), which is associated with an Na^+ diffusion impedance through the SEI layer [45]. This indicates that the carbonate-based liquid electrolyte was not as stable at this voltage window, and excessive electrolyte decomposition over long-term cycling leading to formation of a thick SEI layer was a factor for cycle retention loss.

After 30,000 cycles between 0 and 3 V at 250 mA g^{-1} , the NIC was discharged to 0 V and an *ex-situ* XRD (Fig. S7), XPS (Fig. 5), and

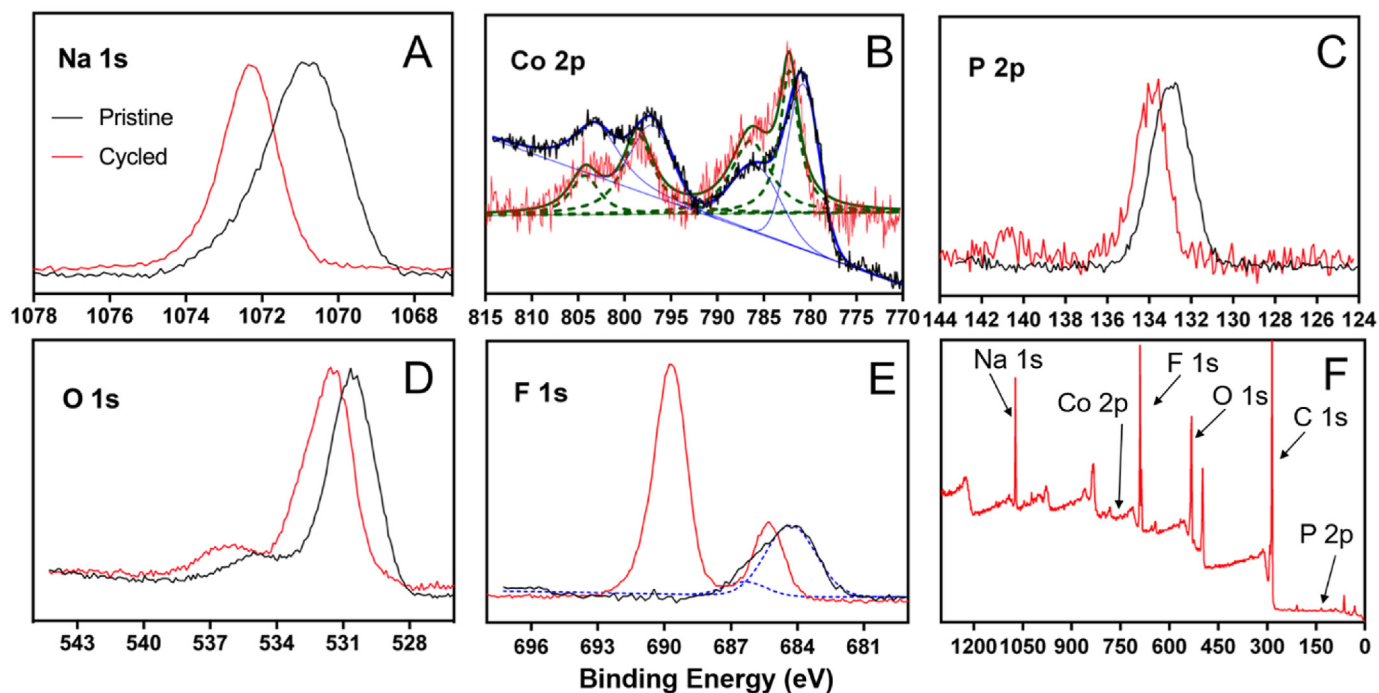


Fig. 5. High-resolution XPS spectra of pristine (black curve) and cycled (red curve) NCPF elements. Peak deconvolution for Co 2p (pristine and cycled) and F 1s (pristine) is shown. (For interpretation of the references to colour in this figure legend, the reader is referred to the Web version of this article.)

EDX (Fig. S8) spectra of the NCPF anode was obtained. The XRD pattern evidently displays low-intensity peaks, but most pristine lattice peaks are observed and crystallinity is remarkably retained compared to the half-cell *ex-situ* pattern shown in Fig. S5. As the half-cell characterization was conducted over a wide voltage range (0–3 V vs Na/Na⁺), structural degradation can be ascribed to irreversible bulk intercalation processes. However, in NIC configuration, NCPF likely operates in a narrower voltage range that primarily involves pseudocapacitance (*i.e.*, limited Na⁺ insertion in the interlayer spacing), which explains the structural preservation over long-term cycling. After cycling, the Na 1s (1072.3 eV, Fig. 5A) and O 1s (532.52 eV, Fig. 5D) XPS spectra appear in disproportionately high intensity and thus are likely associated with SEI layer and electrolyte species deposited on the surface of the electrode (*e.g.*, NaCl, NaClO₄, and Na₂O) [46]. The high-energy F 1s peak (689.8 eV, Fig. 5E) is ascribed to the *p*-CF₂=CF₂ bonds from the Teflon-based binder while the lower energy peak (685.29 eV) may arise from fluoride salts generated from defluorination side reactions with the binder [39]. On the other hand, the Co 2p (Fig. 5B) and P 2p (Fig. 5C) spectra appear in low intensity (Fig. 5F) due to the limited sampling depth of the spectrometer and thus likely correspond to the active material. The Co 2p displays binding energies of 782.25 and 798.55 eV for the 2p_{3/2} and 2p_{1/2} multiplets respectively (16.05 eV orbital splitting), with respective shoulder peaks at 786.42 and 804.28 eV. The valence state is difficult to ascertain due to the poor resolution of the satellite region – the position and relative intensity of the 2p_{3/2} shoulder peak indicates a Co²⁺ state, while the broad appearance suggests a mixed Co²⁺/Co³⁺ state [47]. The upshift in binding energies compared to pristine NCPF can be ascribed to structural changes (Fig. S7) as well as an increased Co–F bond character due to charge balance and potential Na⁺ rearrangement during the oxidation of Co²⁺ [39]. The atomic percent ratio of the active metals Co:P calculated after cycles from the XPS intensities is 1:0.986, indicating stability throughout cycling. In addition, elemental mapping of Co and P (1:0.994 intensity ratio)

from EDX (Fig. S8) shows that the elements are distributed similarly throughout the electrode. These characterizations confirm the electrochemical and mechanical stability of the NCPF anode over extended cycling, thus showcasing its promise toward next-generation NIC devices.

4. Conclusions

In this work, NCPF was synthesized using a two-step technique and tested as an NIC anode for the first time. When functioning as an anode, NCPF demonstrated a pseudocapacitive charge-storage mechanism, allowing it to match the facile adsorption-based kinetics of the AC cathode. This resulted in an excellent cycle stability and rate performance when cycled between 0 and 3 V, achieving a 93% capacitance retention over 100,000 cycles and a 78% retention from a 125 to 5000 W kg⁻¹ power output. The energy density of the device was expanded at a voltage range of 0–3.25 V and demonstrated good cycle retention at a moderate current density (250 mA g⁻¹ or 375 W kg⁻¹). At this voltage range, extensive electrolyte decomposition was a notable factor for cycle retention loss. X-ray spectroscopy characterization of the NCPF anode after long-term cycling confirm its electrochemical and mechanical stability. The performance benchmarks with respect to cyclability and power output of our NCPF//AC device are comparable to supercapacitors, while also demonstrating a considerably higher energy density.

Declaration of competing interest

The authors declare no conflict of interest.

CRediT authorship contribution statement

Tyler Or: Conceptualization, Investigation, Validation, Visualization, Writing - original draft. **Karthikeyan Kaliyappan:**

Conceptualization, Methodology, Writing - review & editing. **Gaoran Li:** Writing - review & editing. **Salah Abureden:** Resources. **Zhengyu Bai:** Supervision, Funding acquisition. **Zhongwei Chen:** Supervision, Funding acquisition.

Acknowledgements

The authors gratefully acknowledge the financial support from the Natural Sciences and Engineering Research Council of Canada (NSERC) and the University of Waterloo. This work was financially supported by the 111 Project (No. D17007). K.K acknowledges the financial support from Henan Normal University, China for this work. T. O was supported through the NSERC Canada Graduate Scholarships-Master's Program.

Appendix A. Supplementary data

Supplementary data to this article can be found online at <https://doi.org/10.1016/j.electacta.2020.136024>.

References

- [1] J. Ding, W. Hu, E. Paek, D. Mitlin, Review of hybrid ion capacitors: from aqueous to lithium to sodium, *Chem. Rev.* 118 (2018) 6457–6498, <https://doi.org/10.1021/acs.chemrev.8b00116>.
- [2] D.P. Dubal, O. Ayyad, P. Gómez-Romero, Hybrid energy storage: the merging of battery and supercapacitor chemistries, *Chem. Soc. Rev.* 34 (2015) 4889–4899.
- [3] S. Deng, J. Li, S. Sun, H. Wang, J. Liu, H. Yan, Synthesis and electrochemical properties of Li₄Ti₅O₁₂ spheres and its application for hybrid supercapacitors, *Electrochim. Acta* 146 (2014) 37–43.
- [4] D. Bauer, A.J. Roberts, N. Matsumi, J.A. Darr, Nano-sized Mo- and Nb-doped TiO₂ as anode materials for high energy and high power hybrid Li-ion capacitors, *Nanotechnology* 28 (2017), 195403, <https://doi.org/10.1088/1361-6528/aa69df>.
- [5] F. Yao, D.T. Pham, Y.H. Lee, Carbon-based materials for lithium-ion batteries, electrochemical capacitors, and their hybrid devices, *ChemSusChem* 8 (2015) 2284–2311.
- [6] N. Arun, A. Jain, V. Aravindan, S. Jayaraman, W. Chui Ling, M.P. Srinivasan, S. Madhavi, Nanostructured spinel LiNi_{0.5}Mn_{1.5}O₄ as new insertion anode for advanced Li-ion capacitors with high power capability, *Nanomater. Energy* 12 (2015) 69–75, <https://doi.org/10.1016/j.nanoen.2014.12.006>.
- [7] K. Karthikeyan, V. Aravindan, S.B. Lee, I.C. Jang, H.H. Lim, G.J. Park, M. Yoshio, Y.S. Lee, A novel asymmetric hybrid supercapacitor based on Li₂FeSiO₄ and activated carbon electrodes, *J. Alloys Compd.* 504 (2010) 224–227, <https://doi.org/10.1016/j.jallcom.2010.05.097>.
- [8] D. Cericola, P. Novák, A. Wokaun, R. Kötz, Hybridization of electrochemical capacitors and rechargeable batteries: an experimental analysis of the different possible approaches utilizing activated carbon, Li₄Ti₅O₁₂ and LiMn₂O₄, *J. Power Sources* 196 (2011) 10305–10313, <https://doi.org/10.1016/j.jpowsour.2011.07.032>.
- [9] S. Dsoke, B. Fuchs, E. Gucciardi, M. Wohlfahrt-Mehrens, The importance of the electrode mass ratio in a Li-ion capacitor based on activated carbon and Li₄Ti₅O₁₂, *J. Power Sources* 282 (2015) 385–393, <https://doi.org/10.1016/j.jpowsour.2015.02.079>.
- [10] J. Ding, H. Wang, Z. Li, K. Cui, D. Karpuzov, X. Tan, A. Kohandehghan, D. Mitlin, Peanut shell hybrid sodium ion capacitor with extreme energy-power rivals lithium ion capacitors, *Energy Environ. Sci.* 8 (2015) 941–955, <https://doi.org/10.1039/c4ee02986k>.
- [11] R. Thangavel, B. Moorthy, D.K. Kim, Y.-S. Lee, Pushing the energy output and cyclability of sodium hybrid capacitors at high power to new limits, *Adv. Energy Mater.* 7 (2017), 1602654, <https://doi.org/10.1002/aenm.201602654>.
- [12] R. Thangavel, K. Kaliyappan, K. Kang, X. Sun, Y.-S. Lee, Going beyond lithium hybrid capacitors: proposing a new high-performing sodium hybrid capacitor system for next-generation hybrid vehicles made with bio-inspired activated carbon, *Adv. Energy Mater.* 6 (2016), 1502199, <https://doi.org/10.1002/aenm.201502199>.
- [13] K. Kaliyappan, Z. Chen, Atomic-scale manipulation of electrode surface to construct extremely stable high-performance sodium ion capacitor, *Nanomater. Energy* 48 (2018) 107–116, <https://doi.org/10.1016/j.nanoen.2018.03.021>.
- [14] Q. Qu, Y. Zhu, X. Gao, Y. Wu, Core-Shell structure of polypyrrole grown on V₂O₅ nanoribbon as high performance anode material for supercapacitors, *Adv. Energy Mater.* 2 (2012) 950–955, <https://doi.org/10.1002/aenm.201200088>.
- [15] H. Li, J. Lang, S. Lei, J. Chen, K. Wang, L. Liu, T. Zhang, W. Liu, X. Yan, A high-performance sodium-ion hybrid capacitor constructed by metal-organic framework-derived anode and cathode materials, *Adv. Funct. Mater.* 28 (2018), 1800757, <https://doi.org/10.1002/adfm.201800757>.
- [16] H. Vikström, S. Davidsson, M. Höök, Lithium availability and future production outlooks, *Appl. Energy* 110 (2013) 252–266, <https://doi.org/10.1016/j.apenergy.2013.04.005>.
- [17] T. Wei, G. Yang, C. Wang, Iso-Oriented NaTi₂(PO₄)₃ mesocrystals as anode material for high-energy and long-durability sodium-ion capacitor, *ACS Appl. Mater. Interfaces* 9 (2017) 31861–31870, <https://doi.org/10.1021/acsami.7b08778>.
- [18] Y.-E. Zhu, L. Yang, J. Sheng, Y. Chen, H. Gu, J. Wei, Z. Zhou, Fast sodium storage in TiO₂@CNT@C nanorods for high-performance Na-ion capacitors, *Adv. Energy Mater.* 7 (2017), 1701222, <https://doi.org/10.1002/aenm.201701222>.
- [19] J.W. Kim, V. Augustyn, B. Dunn, The effect of crystallinity on the rapid pseudocapacitive response of Nb₂O₅, *Adv. Energy Mater.* 2 (2012) 141–148, <https://doi.org/10.1002/aenm.201100494>.
- [20] S. Dong, L. Shen, H. Li, P. Nie, Y. Zhu, Q. Sheng, X. Zhang, Pseudocapacitive behaviours of Na₂Ti₃O₇@CNT coaxial nanocables for high-performance sodium-ion capacitors, *J. Mater. Chem. A* 3 (2015) 21277–21283, <https://doi.org/10.1039/c5ta05714k>.
- [21] K. Kubota, K. Yokoh, N. Yabuuchi, S. Komaba, Na₂CoPO₄F as a high-voltage electrode material for Na-ion batteries, *Electrochemistry* 82 (2014) 909–911, <https://doi.org/10.5796/electrochemistry.82.909>.
- [22] H. Zou, S. Li, X. Wu, M.J. McDonald, Y. Yang, Spray-drying synthesis of pure Na₂CoPO₄F as cathode material for sodium ion batteries, *ECS Electrochem. Lett.* 4 (2015) A53–A55, <https://doi.org/10.1149/2.0061506eel>.
- [23] F. Sanz, C. Parada, C. Ruiz-Valero, Crystal growth, crystal structure and magnetic properties of disodium cobalt fluorophosphate, *J. Mater. Chem.* 11 (2001) 208–211, <https://doi.org/10.1039/b003150j>.
- [24] R. Ling, S. Cai, S. Shen, X. Hu, D. Xie, F. Zhang, X. Sun, N. Yu, F. Wang, Synthesis of carbon coated Na₂FePO₄F as cathode materials for high-performance sodium ion batteries, *J. Alloys Compd.* 704 (2017) 631–640, <https://doi.org/10.1016/j.jallcom.2017.02.075>.
- [25] N.R. Khasanova, O.A. Drozhzhin, D.A. Storozhilova, C. Delmas, E.V. Antipov, New form of Li₂FePO₄F as cathode material for Li-ion batteries, *Chem. Mater.* 24 (2012) 4271–4273, <https://doi.org/10.1021/cm302724a>.
- [26] B.L. Ellis, W.R.M. Makahnouk, W.N. Rowan-Weetaluktuk, D.H. Ryan, L.F. Nazar, Crystal structure and electrochemical properties of A₂MPO₄F fluorophosphates (A = Na, Li; M = Fe, Mn, Co, Ni)[†], *Chem. Mater.* 22 (2010) 1059–1070, <https://doi.org/10.1021/cm902023h>.
- [27] N. Recham, J.N. Chotard, J.C. Jumas, L. Laffont, M. Armand, J.M. Tarasco, Ion-thermal synthesis of Li-based fluorophosphates electrodes, *Chem. Mater.* 22 (2010) 1142–1148, <https://doi.org/10.1021/cm9021497>.
- [28] L. Lutterotti, Total pattern fitting for the combined size–strain–stress–texture determination in thin film diffraction, *Nucl. Instrum. Methods Phys. Res. Sect. B Beam Interact. Mater. Atoms* 268 (2010) 334–340, <https://doi.org/10.1016/j.nimb.2009.09.053>.
- [29] K. Momma, F. Izumi, IUCr, VESTA 3 for three-dimensional visualization of crystal, volumetric and morphology data, *J. Appl. Crystallogr.* 44 (2011) 1272–1276, <https://doi.org/10.1107/S0021889811038970>.
- [30] R. Hammond, J. Barbier, Structural Chemistry of NaCoPO₄, *Acta Crystallogr. Sect. B Struct. Sci.* 52 (1996) 440–449, <https://doi.org/10.1107/S0108768195016259>.
- [31] F. Croce, A. D'Epifanio, J. Hassoun, A. Deptula, T. Olczac, B. Scrosati, A novel concept for the synthesis of an improved LiFePO₄[sub 4] lithium battery cathode, *Electrochim. Solid State Lett.* 5 (2002) A47, <https://doi.org/10.1149/1.1449302>.
- [32] D. Wang, J. Xiao, W. Xu, Z. Nie, C. Wang, G. Graff, J.G. Zhang, Preparation and electrochemical investigation of Li₂CoPO₄F cathode material for lithium-ion batteries, *J. Power Sources* 196 (2011) 2241–2245, <https://doi.org/10.1016/j.jpowsour.2010.10.021>.
- [33] K. Kaliyappan, Z. Chen, Facile solid-state synthesis of eco-friendly sodium iron silicate with exceptional sodium storage behaviour, *Electrochim. Acta* 283 (2018) 1384–1389, <https://doi.org/10.1016/j.electacta.2018.07.034>.
- [34] J. Moulder, W. Stickle, P. Sobol, K. Bomben, Handbook of X-ray photoelectron spectroscopy, <https://doi.org/10.1002/sia.740030412>, 1995.
- [35] Q.H. Wu, A. Thißen, W. Jaegermann, XPS and UPS study of Na deposition on thin film V₂O₅, *Appl. Surf. Sci.* 252 (2005) 1801–1805, <https://doi.org/10.1016/j.apsusc.2005.03.134>.
- [36] Q. Li, Z. Liu, F. Zheng, R. Liu, J. Lee, G.L. Xu, G. Zhong, X. Hou, R. Fu, Z. Chen, K. Amine, J. Mi, S. Wu, C.P. Grey, Y. Yang, Identifying the structural evolution of the sodium ion battery Na₂FePO₄F cathode, *Angew. Chem. Int. Ed.* 57 (2018) 11918–11923, <https://doi.org/10.1002/anie.201805555>.
- [37] S. Okada, M. Ueno, Y. Uebou, J.I. Yamaki, Fluoride phosphate Li₂CoPO₄F as a high-voltage cathode in Li-ion batteries, *J. Power Sources* 146 (2005) 565–569, <https://doi.org/10.1016/j.jpowsour.2005.03.149>.
- [38] C. Wei, C. Cheng, B. Zhou, X. Yuan, T. Cui, S. Wang, M. Zheng, H. Pang, Hierarchically porous NaCoPO₄-Co₃O₄ hollow microspheres for flexible asymmetric solid-state supercapacitors, *Part. Part. Syst. Char.* 32 (2015) 831–839, <https://doi.org/10.1002/ppsc.201500018>.
- [39] R.A. Quinlan, Y.-C. Lu, D. Kwabi, Y. Shao-Horn, A.N. Mansour, XPS investigation of the electrolyte induced stabilization of LiCoO₂ and “AlPO₄ 4”-Coated LiCoO₂ composite electrodes, *J. Electrochem. Soc.* 163 (2016) A300–A308, <https://doi.org/10.1149/2.0851602jes>.
- [40] T. Brezesinski, J. Wang, S.H. Tolbert, B. Dunn, Ordered mesoporous α-MoO₃ with iso-oriented nanocrystalline walls for thin-film pseudocapacitors, *Nat. Mater.* 9 (2010) 146–151, <https://doi.org/10.1038/nmat2612>.

- [41] J. Wang, J. Polleux, J. Lim, B. Dunn, Pseudocapacitive contributions to electrochemical energy storage in TiO₂(anatase) nanoparticles, *J. Phys. Chem. C* 111 (2007) 14925–14931, <https://doi.org/10.1021/jp074464w>.
- [42] A. Gutierrez, S. Kim, T.T. Fister, C.S. Johnson, Microwave-assisted synthesis of NaCoPO₄ red-phase and initial characterization as high voltage cathode for sodium-ion batteries, *ACS Appl. Mater. Interfaces* 9 (2017) 4391–4396, <https://doi.org/10.1021/acsami.6b14341>.
- [43] J. Shu, Electrochemical behavior and stability of Li₄Ti₅O₁₂ in a broad voltage window, *J. Solid State Electrochem.* 13 (2009) 1535–1539, <https://doi.org/10.1007/s10008-008-0723-z>.
- [44] M. Huang, A. Xu, H. Duan, S. Wu, Enhanced pseudocapacitance contribution to outstanding Li-storage performance for a reduced graphene oxide-wrapped FeS composite anode, *J. Mater. Chem. A* 6 (2018) 7155–7161, <https://doi.org/10.1039/C8TA00740C>.
- [45] S.S. Zhang, K. Xu, T.R. Jow, EIS study on the formation of solid electrolyte interface in Li-ion battery, *Electrochim. Acta* 51 (2006) 1636–1640, <https://doi.org/10.1016/j.electacta.2005.02.137>.
- [46] L. Bodenes, A. Darwiche, L. Monconduit, H. Martinez, The Solid Electrolyte Interphase a key parameter of the high performance of Sb in sodium-ion batteries: comparative X-ray Photoelectron Spectroscopy study of Sb/Na-ion and Sb/Li-ion batteries, *J. Power Sources* 273 (2015) 14–24, <https://doi.org/10.1016/j.jpowsour.2014.09.037>.
- [47] L. Dahéron, R. Dedryvère, H. Martinez, M. Ménétrier, C. Denage, C. Delmas, D. Gonbeau, Electron transfer mechanisms upon lithium deintercalation from LiCoO₂ to CoO₂ investigated by XPS, *Chem. Mater.* 20 (2008) 583–590, <https://doi.org/10.1021/cm702546s>.